ADVANCED MATERIALS
www.advmat.de

Core–Shell Perovskite Quantum Dots for Highly Selective Room-Temperature Spin Light-Emitting Diodes

Gyumin Jang, Dae-Yeon Jo, Sunihl Ma, Junwoo Lee, Jaehyun Son, Chan Uk Lee, Wooyong Jeong, Seongyeon Yang, Jeong Hyun Park, Heesun Yang, and Jooho Moon**

Circularly polarized light (CPL) is a crucial light source with a wide variety of potential applications such as magnetic recording, and 3D display. Here, core–shell heterostructured perovskite quantum dots (QDs) for room-temperature spin-polarized light-emitting diodes (spin-LEDs) are developed. Specifically, a 2D chiral perovskite shell is deposited onto the achiral 3D inorganic perovskite ($CsPbBr_3$) core. Owing to the chiral-induced spin selectivity effect, the spin state of the injected charge carriers is biased when they are transmitted through the 2D chiral shell. The spin-controlled carriers then radiatively recombine inside the $CsPbBr_3$ emissive core, resulting in CPL emission. It is demonstrated that the (*R*)- and (*S*)-1-(2-(naphthyl)ethylamine) (*R*-/*S*-NEA) 2D chiral cations enhance the spin polarization degree due to their strong chiroptical properties. Systematical defect analyses confirm that 2D chiral cations (i.e., *R*-/*S*-NEA) successfully passivate halide vacancies at the surface of the $CsPbBr_3$ QDs, thereby attaining a high photoluminescence quantum yield of 78%. Moreover, the spin-LEDs prepared with core–shell QDs achieve a maximum external quantum efficiency of 5.47% and circularly polarized electroluminescence with a polarization degree ($P_{CP\text{-}EL}$) of 12% at room temperature. Finally, various patterns fabricated by inkjet printing the core–shell QDs emit strong CPL, highlighting their potential as an emitter for next-generation displays.

1. Introduction

Circularly polarized light (CPL) is elliptically polarized light that consists of two orthogonal electromagnetic plane waves of identical magnitude and 90° difference in phase. CPL functions as a light source for a wide variety of applications, such as magnetic recording, 3D display, information processing, and quantum-based optical computing.[1–4] Typically, CPL can be artificially generated through the integration of semiconductors and ferromagnets, which facilitates the control of spin populations.[5,6] In the absence of a magnetic field, the spin populations can be adjusted using chiral semiconductors through the chiral-induced spin selectivity (CISS) effect.[7,8] In this case, the spin of the transmitting carriers is polarized so as to allow only one of the spin states (i.e., either the up- or down-spin state). Among various classes of chiral semiconductors, 2D chiral organic–inorganic hybrid perovskites (2D chiral OIHPs) have been extensively investigated since the first report in 2017 owing to their exceptional spin-related properties.[9–14] In addition to the polarization effect, the extraordinary optoelectronic properties such as large Rashba splitting and strong spin–orbit coupling make them fascinating candidate for the CPL emitter.[15–18] Nevertheless, the 2D chiral OIHPs can hardly be directly applied as an emitter due to their exceedingly high bandgap and electrically insulating nature.[19]

Recently, Kim et al. realized developed room-temperature spin-polarized light-emitting diodes (spin-LEDs). In this framework, 2D chiral OIHP film was deposited at the bottom of a $CsPbI_3$ quantum dot (QD) emitter to function as a spin-filter layer through the CISS effect.[20] This approach helped overcome the electrical limitation of 2D chiral OIHPs, and the resulting spin-LEDs exhibited a circularly polarized electroluminescence (CP-EL) dissymmetry factor ($g_{CP\text{-}EL}$) of 5.2×10^{-3}. However, the short spin-coherence time in the ambient condition likely reduced the spin selectivity, which limited the maximum thickness of the emissive $CsPbI_3$ QD layer to ≈20 nm. Therefore, the luminescence of the prepared spin-LEDs was weak due to the scarceness of emitting materials. To fully exploit the remarkable chiral-induced properties of 2D chiral OIHPs, the CISS layer, emitting materials, and their physical structures must be appropriately selected and designed considering the limited spin lifetime of the injected carriers.

G. Jang, S. Ma, J. Lee, J. Son, C. U. Lee, W. Jeong, S. Yang, J. H. Park, J. Moon
Department of Materials Science and Engineering
Yonsei University
Seoul 03722, Republic of Korea
E-mail: jmoon@yonsei.ac.kr
D.-Y. Jo, H. Yang
Department of Materials Science and Engineering
Hongik University
Seoul 04066, Republic of Korea
E-mail: hyang@hongik.ac.kr
S. Ma
Department of Chemical Engineering
University of Michigan
Ann Arbor, MI 48109, USA

The ORCID identification number(s) for the author(s) of this article can be found under https://doi.org/10.1002/adma.202309335

DOI: 10.1002/adma.202309335

In this study, we prepared room-temperature spin-LEDs based on core–shell perovskite QDs. The core of the QDs consisted of achiral inorganic 3D perovskite ($CsPbBr_3$), which functioned as highly luminescent emitting materials. The shell was designed as a CISS layer based on 2D chiral OIHPs, in which the spin state of injected charge carriers was biased according to the handedness of the chiral perovskite. Notably, Ye et al. also reported core–shell structured perovskite nanocrystals with type-II band alignment for room-temperature spin-LEDs.[21] However, the quasi-2D perovskite used as a CISS layer suffered from weak spin selectivity, presumably because of the penetration of the chiral organic cation into the methylammonium lead bromide core QDs during the synthesis, which significantly impaired the polarization degree of the emission. Moreover, organic cations with lengthy carbon chains cannot be easily incorporated into cesium lead halide perovskites.[22] Considering these aspects, we used $CsPbBr_3$ QDs, which helped generate a discrete boundary between the core and shell. Because chiral organic cations typically form a chirality-induced spin control shell, (*R*)- and (*S*)-1-(2-(naphthyl)ethylamine) (denoted as *R*- and *S*-NEA, respectively) were introduced instead of conventional (*R*)- and (*S*)-methylbenzylamine (denoted as *R*- and *S*-MBA, respectively). The introduction of *R*-/*S*-NEA chiral cations enhanced the spin polarization property owing to their higher magnetic transition dipole moment (MTDM).[23] In addition, the *R*-/*S*-NEA chiral cations increased the quantum efficiencies of the core–shell QDs. Systematical quantitative defect analyses revealed that the luminescence was enhanced owing to the defect healing induced by the *R*-/*S*-NEA cations. Owing to the defect passivation, the core–shell QDs with the *R*-/*S*-NEA shell exhibited a high photoluminescence quantum yield (PLQY) of 78%. We fabricated spin-LEDs in which the preferred spin state of the injected electrons was successfully regulated by the handedness of the 2D chiral OIHP shell. The resulting spin-LEDs exhibited a maximum external quantum efficiency (EQE) of 5.47% and $|g_{CP\text{-}EL}|$ of 2.4×10^{-1} at room temperature. Finally, the core–shell QD ink was transferred to the inkjet printer and used to generate various patterns that emitted strong CPL that could be visually detected.

2. Results and Discussion

The $FAPbBr_3$ and $CsPbBr_3$ QDs were fabricated by the ligand-assisted reprecipitation and hot-injection methods, respectively (details are presented in the Experimental Section).[24,25] After synthesis and purification, each QD was redispersed in a nonpolar solvent (i.e., toluene) to generate the 2D chiral OIHP shell. A stoichiometric precursor solution was prepared by dissolving equimolar chiral organic cations (i.e., either *R*-/*S*-MBA or *R*-/*S*-NEA) and lead halide in *N*,*N*-dimethylformamide (DMF), followed by dropwise injection into either a $FAPbBr_3$ or $CsPbBr_3$ QD dispersion under vigorous stirring. **Figure 1**a,b shows the photoluminescence (PL) and absorbance spectra for the prepared core–shell QD dispersions, which were obtained with an excitation laser wavelength of 300 nm to examine the optical properties. Dominant PL emission peaks were observed at ≈540 and 510 nm, consistent with the previously reported optical bandgaps of $FAPbBr_3$ (≈2.3 eV) and $CsPbBr_3$ (≈2.4 eV), respectively.[24,25] The PL emission peak positions of the $FAPbBr_3$ and $CsPbBr_3$ core–shell QDs did not change significantly as the molar concentration of the shell precursor increased from 0 to 2 mM Pb. In both cases, the PL peaks corresponding to the shell were not detected owing to the scarceness and weak luminescence of 2D chiral OIHP materials. The intensity of the PL peak for the $FAPbBr_3$ QDs decreased dramatically as the shell precursor concentration increased. The PL peak intensity was negligible at a concentration of 1 mM, and the luminescence completely disappeared when the molar concentration reached 2 mM (Figure 1c). This observation indicated that the 2D shell precursor likely interacted with the $FAPbBr_3$ core QDs during the growth of the shell layer. The chiral cations likely penetrated the $FAPbBr_3$ core lattice due to their miscibility, resulting in recrystallization from the surfaces of 3D $FAPbBr_3$ through the generation of various quasi-2D perovskite phases ($n = 1, 2, 3,\ldots$).[26,27] Therefore, the excellent luminescence of the 3D perovskite (i.e., $FAPbBr_3$) deteriorated because a large part of the luminescent core was converted to the quasi-2D chiral OIHPs that exhibit stronger electron–phonon coupling and a larger optical bandgap. Similarly, the CISS effect of the shell was likely weakened owing to the reduced spin polarization ability of the quasi-2D chiral OIHPs, because the loss of the chiral organic cation inside the shell limited the spin selectivity of the shell.[28] The absorbance spectra of the $FAPbBr_3$ core–shell QDs prepared with a shell precursor concentration of 1 mM (Figure 1a, gray line) confirmed the existence of diverse 2D phases in the QDs owing to the penetration of the chiral organic cations. The absorption peaks at 395 and 490 nm corresponded to the 2D phases of $n = 1$ and 4, respectively, and that at 545 nm corresponded to the absorption edge for $FAPbBr_3$.[29]

By contrast, in the case of the inorganic $CsPbBr_3$ core–shell QDs, the luminescence property doubled in terms of the PL intensity after the injection of the shell precursor with a concentration of 1 mM. The luminescence was further enhanced when the shell precursor concentration increased to 2 mM (Figure 1d), as discussed later. As expected, the absorbance spectra of the $CsPbBr_3$ colloidal dispersion injected with the 1 mM shell precursor (Figure 1b, gray line) exhibited only two absorption peaks at 370 and 510 nm, attributable to the $n = 1$ MBA_2PbBr_4 2D phase and $CsPbBr_3$, respectively. In order to exclude the possibility of the independent 2D perovskite QD formation, we conducted dynamic light scattering (DLS) measurement. As demonstrated in Figure S1 (Supporting Information), DLS result of $CsPbBr_3$ core QD solution displayed sharp peak intensity, indicating their excellent size uniformity. Similarly, DLS spectra of core–shell structured QDs fabricated with *R*-NEA-based shell exhibited monomodal distribution along with slightly broader size distribution. Therefore, it can be conjectured that only core–shell QDs without any other separate 2D QDs were generated inside the final QD dispersion. Furthermore, we obtained X-ray diffraction (XRD) spectra of core–shell QD films in order to gain additional evidence for the evolution of a 2D chiral shell on $CsPbBr_3$ QDs (Figure S2, Supporting Information). In addition to the peaks corresponding to $CsPbBr_3$ core, diffraction peaks assignable for layered 2D perovskite structure was recognizable. Therefore, it can be affirmed that the increased particle size identified by DLS measurements (Figure S1, Supporting Information) obviously results from the deposition of a 2D perovskite shell around the $CsPbBr_3$ core. According to a previous study, bulky 2D organic cations (i.e., MBA in this case) cannot be incorporated into the lattice of inorganic cesium lead halide perovskites.[22] Therefore, it can be

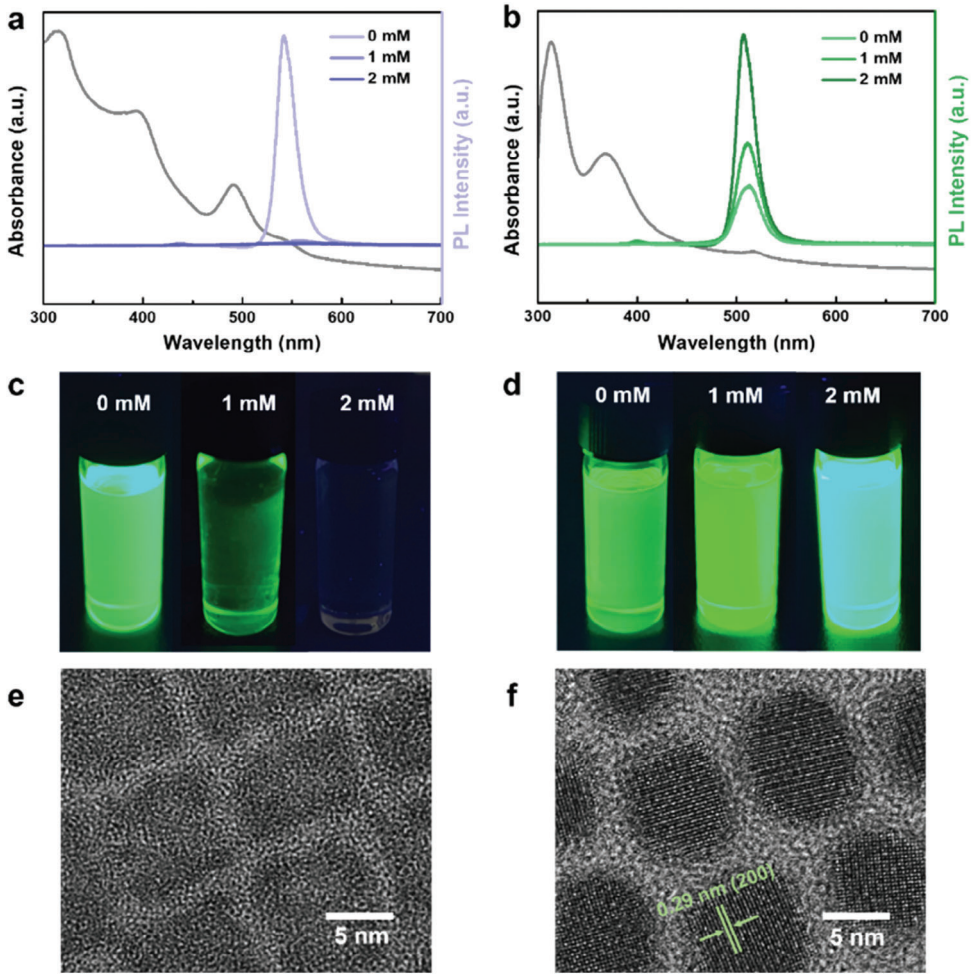

Figure 1. Absorbance and steady-state PL spectra of a) $FAPbBr_3$ and b) $CsPbBr_3$ QD solutions with varying concentrations of MBA shell precursor. Digital photographs of c) $FAPbBr_3$ and d) $CsPbBr_3$ QD solutions with increasing concentration of shell precursor under UV light. HRTEM images of core–shell structured e) $FAPbBr_3$ and f) $CsPbBr_3$ QDs with shells consisting of *R*-/*S*-MBA-based 2D chiral OIHPs.

speculated that 2D chiral cations typically do not penetrate the 3D $CsPbBr_3$ core lattice. In general, to fabricate spin-LEDs with high selectivity, the spin filtering effect of the CISS layer (i.e., the chiral shell) and the luminescence of the emissive core must be simultaneously improved. Our findings highlighted that the $CsPbBr_3$ QDs can be used to produce core–shell QDs with a distinct heterojunction for high-performance spin-LEDs with a strong spin polarization property.

High-resolution transmission electron microscopy (HRTEM) images of the $FAPbBr_3$ and $CsPbBr_3$ core–shell QDs were captured. As shown in Figure 1e,f, both the QDs were rectangular with a similar diameter of ≈12 nm. However, the boundary between the core and shell was quite ambiguous in the case of the $FAPbBr_3$ QDs, and the lattice structure of the $FAPbBr_3$ could not be recognized (Figure 1e). HRTEM image of the $CsPbBr_3$ core QDs without shell is also demonstrated in Figure S3 (Supporting Information), exhibiting their average size of ≈8 nm. Considering that the diameter of core–shell structured QDs was ≈12 nm (Figure 1f), the thickness of shell could be estimated to be ≈2 nm. The obscurity of the lattice structure could be attributed to the penetration of the 2D chiral cation into the $FAPbBr_3$ cores. By contrast, the lattice structure of the $CsPbBr_3$ QDs could be clearly identified with a representative lattice spacing of 0.29 nm corresponding to the (200) plane.[30,31] Additionally, a moderately distinct boundary could be recognizable between the core $CsPbBr_3$ and 2D-chiral-OIHP-based shell by their brightness difference. The observation of a relatively definite interface distinguished by brightness difference assures the excellent luminescence properties of $CsPbBr_3$ core–shell QDs. It is noteworthy that the introduction of 2D chiral precursors did not disrupt the lattice structure of the core QDs (Figure 1b), in contrast to the $FAPbBr_3$ QDs. These results demonstrated that inorganic perovskite QDs can be used for constructing core–shell QDs with well-defined heterostructures. Meanwhile, in both cases, it was challenging to observe the lattice spacing of the shell, which is highly consistent with previous reports.[32,33] During the early stage of TEM analysis with $CsPbBr_3$ core–shell QDs, it was possible to observe slight trace of 2D perovskite layered structure, as shown in Figure S4 (Supporting Information). At later stage, the layered structure of 2D perovskite was deteriorated during high magnification TEM analysis, because the large organic portion in the 2D chiral OIHPs led to structural instability under intense electron beam.

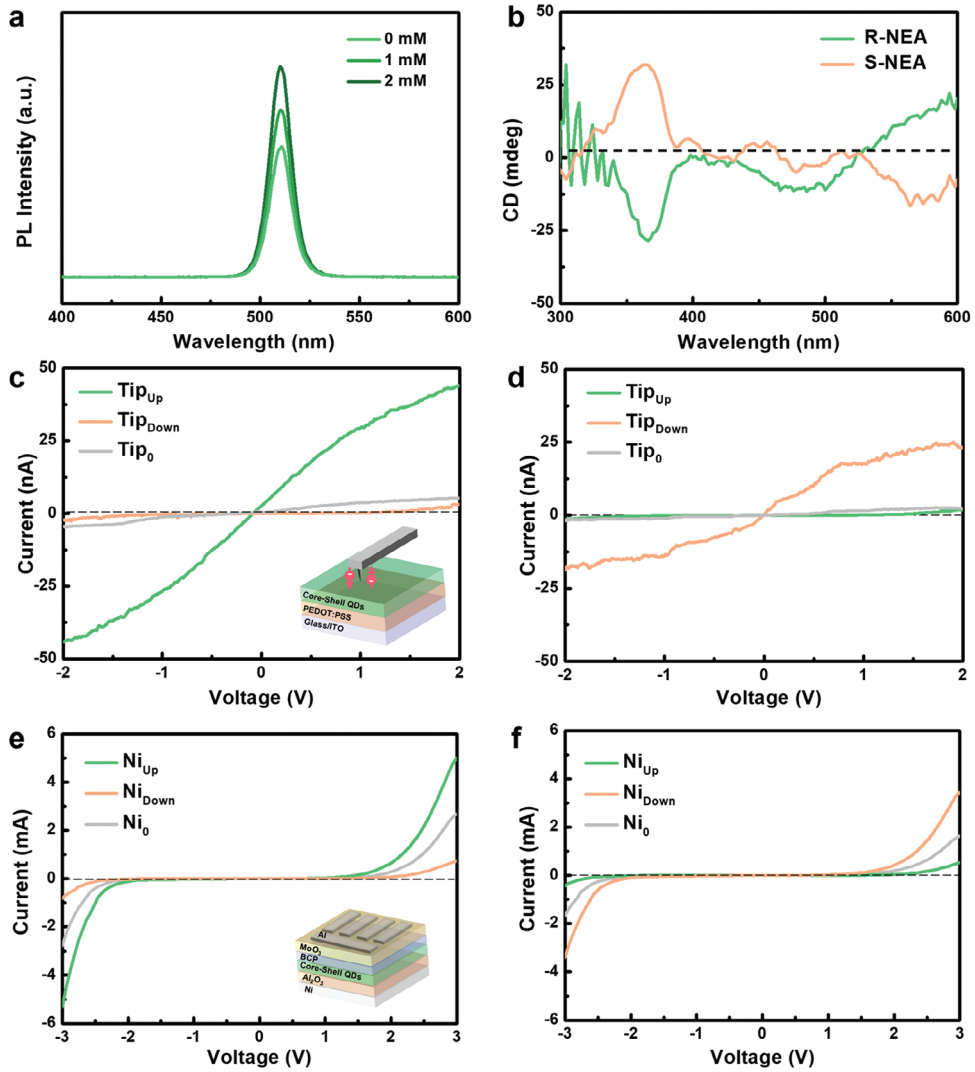

Figure 2. a) Steady-state PL spectra of $CsPbBr_3$ QD solutions with varying concentrations of NEA shell precursor. b) CD spectra of core–shell QDs prepared with *R*-/*S*-NEA 2D chiral cation. Current–voltage responses of c) ITO/PEDOT:PSS/$CsPbBr_3$ QD films with *R*-NEA 2D chiral OIHP shell and d) ITO/PEDOT:PSS/$CsPbBr_3$ QD films with *S*-NEA 2D chiral OIHP shell, obtained by mCP-AFM at room temperature. Average current–voltage characteristics measured with e) *R*-NEA and f) *S*-NEA-based CISS devices. The current–voltage curves were obtained 10 times with each CISS device under opposite magnetization direction of the Ni electrode.

It should be also noted that, in most cases, the boundary between core and shell layer can rarely be distinguishable by HRTEM images regardless of the material types due to the epitaxial growth of shell materials on core.[34–37] Therefore, X-ray photoelectron spectroscopy (XPS) was conducted in order to further confirm the evolution of core–shell QDs. The Pb 4f, Br 3d, and Cs 3d XPS spectra are also demonstrated in Figure S5 (Supporting Information). The intensity of Cs 3d peak in core–shell QDs spectra is significantly lower compared to that of the core QDs, which further confirms the successful deposition of shell around the core QDs (i.e., $CsPbBr_3$). As demonstrated in Table S1 (Supporting Information), XPS surface analysis of $CsPbBr_3$ core QDs revealed that the atomic percentage for Cs was 21.14%, which dramatically decreased to 7.99% after the injection of 2D perovskite (i.e., NEA_2PbBr_4) precursor because Cs-related photoelectron signal from core domain became substantially attenuated by the 2D chiral shell formation without Cs element. This clearly indicates that the 2D chiral shell well surrounded the $CsPbBr_3$ core QDs.

The chiroptical and spin-related properties of 2D chiral OIHPs are influenced by the type of chiral organic cations. We previously observed that the higher MTDM of *R*-/*S*-NEA-based 2D chiral OIHP films resulted in stronger chiral activity compared with those of the films prepared with conventional *R*-/*S*-MBA cations.[23] Therefore, in this study, we synthesized core–shell heterostructured QDs with *R*-/*S*-NEA chiral cations (Figure S6, Supporting Information), whose chiroptical property is expected to be superior to those of core–shell QDs with *R*-/*S*-MBA-based shells. The PL spectra of *R*-NEA-2D-chiral-perovskite-based core–shell QDs were obtained with different molar concentrations of the shell precursor (**Figure 2a**). The PL spectra were similar to those of the *R*-/*S*-MBA-based core–shell QDs: the PL peak intensity strengthened with the increasing shell precursor

concentration. The absorbance spectrum of the $CsPbBr_3$ colloidal dispersion injected with the 1 mM NEA shell precursor (Figure S7, Supporting Information) was also collected. Only two absorption peaks at 395 and 503 nm were detected which can be assigned to $n = 1$ NEA_2PbBr_4 2D phase and $CsPbBr_3$, respectively. The PLQY values for the core $CsPbBr_3$ and core–shell QDs with *R*-NEA 2D chiral shell were measured to quantitatively compare the luminescence. The PLQY increased from 71% to 78% after the injection of the shell precursor with a concentration of 2 mM. These results confirmed that 2D cations cannot penetrate the core, regardless of the chiral cation type, when inorganic $CsPbBr_3$ perovskite QDs are used. Figure 2b shows the circular dichroism (CD) spectra of the colloidal dispersion of the core–shell chiral perovskite QDs based on the *R*-/*S*-NEA chiral cation. As expected, a monosignate mirror-image spectra resulting from the Cotton effect at the absorption band edge of the shell perovskite ($n = 1$ *R*-/*S*-NEA_2PbBr_4) was observed, which is highly consistent with the previous reports.[38,39] Figure S8 (Supporting Information) shows the CD and absorbance spectra of the colloidal dispersion of the core–shell QDs prepared with the *R*-/*S*-MBA-based shell. The CD peak intensity was lower than that of the core–shell QDs with the NEA shell, consistent with the previous reports.[23] Additionally, the CD spectra of the QDs with the racemic (*rac*)-NEA-based 2D chiral OIHP shells were obtained, revealing no CD signal (Figure S9, Supporting Information). To quantitatively evaluate the enhanced chiroptical activity resulting from the different 2D chiral cations, the asymmetry factor (g_{CD}) was calculated using the following equation:

$$g_{CD} = \frac{CD}{(32980 \times \text{absorbance})} \quad (1)$$

The CD and absorbance values were acquired from the CD and absorbance spectra, respectively. As shown in Figure S10 (Supporting Information), the local maximum values of g_{CD} around the optical bandgap of the *R*-MBA and *R*-NEA-based 2D chiral OIHP shells were 1.3×10^{-3} and 2.1×10^{-3}, respectively. The enhanced chiroptical property of the core–shell QDs prepared with NEA chiral cation was verified by the increased maximum g_{CD}, which was almost 1.6 times that of the MBA-cation-based core–shell QDs.

As demonstrated in Figure 2c,d, the core–shell QD films were examined through magnetic conductive-probe atomic force microscopy (mCP-AFM) to investigate the spin-controlled charge transport according to the handedness of the 2D chiral shell. For the measurement, samples with a configuration of indium tin oxide (ITO)/poly(3,4-ethylenedioxythiophene)polystyrenesulfonate (PEDOT:PSS)/core–shell chiral QD films were prepared. It was confirmed that the thickness of core–shell chiral QD film was ≈50 nm by cross-sectional scanning electron microscopy image (Figure S11, Supporting Information). Before scanning, ferromagnetic Co–Cr-coated AFM tips were premagnetized by an external permanent magnet with opposite directions (i.e., magnetized up or down). After the injection of charge carriers through the ITO substrate, they were perpendicularly transferred to the PEDOT:PSS hole injection layer. When the carriers finally reached the QD films through multiple quantum well-structured 2D chiral OIHPs, their spin states were aligned before they were transmitted to the magnetized AFM tip, and anisotropic current was observed depending on the magnetization direction of the AFM tip (Figure 2c). The core–shell QD films with the *R*-NEA shell exhibited considerably stronger current when the tip was magnetized up (44.00 nA at 2 V) than when the tip was either magnetized down (3.22 nA at 2 V) or nonmagnetized (5.77 nA at 2 V). The opposite tendency was observed when core–shell chiral QD films with the *S*-NEA shell were used (Figure 2d): the current was stronger when the tip was magnetized down (23.25 nA at 2 V) compared with when it was magnetized up (1.84 nA at 2 V) or nonmagnetized (2.33 nA at 2 V). The raw data of mCP-AFM measured for 100 times for each condition are displayed in Figure S12 (Supporting Information). Also, 95% confidence limits calculated for all average values are demonstrated in Figure S13 (Supporting Information). Furthermore, the *rac*-NEA-based core–shell chiral QD films displayed negligible difference in current with the magnetization direction of the Co–Cr-coated AFM tips (Figure S14, Supporting Information). The degree of polarized spin current, P_{spin}, was calculated as

$$P_{spin} = \frac{I_{up} - I_{down}}{I_{up} + I_{down}} \times 100\% \quad (2)$$

where I_{up} and I_{down} are the current values measured when the Co–Cr-coated AFM tips were magnetized up and down, respectively. P_{spin} was calculated to be +86.4% and −81.8% for the samples prepared with $CsPbBr_3$ QDs with *R*- and *S*-NEA 2D chiral shells, respectively. Notably, the P_{spin} value measured with the proposed core–shell chiral QD films was higher than those of the previous works.[20] The enhanced P_{spin} value was attributable to the increase in the population of the spin-controlled carriers inside the core–shell QD films.

The mCP-AFM measurements highlight the local characteristics of the core–shell QD film. To demonstrate the reliability of the system in different regions, we constructed CISS devices that contained a ferromagnetic Ni layer and had a large detection area. The CISS devices had a configuration of glass/Ni/Al_2O_3/core–shell QDs with *R*-/*S*- or *rac*-NEA-based 2D chiral shell/bathocuproine (BCP)/molybdenum trioxide (MoO_3)/Al (details can be found in the Experimental Section). Instead of the Co–Cr-coated AFM tips, the bottom Ni layer was premagnetized by a permanent external magnet before obtaining the *I*–*V* curves. When the charge carriers were injected into the magnetized Ni layer, carriers with only one spin direction could pass through. The Al_2O_3 layer functioned as a spin tunneling buffer layer, which helped overcome the spin injection barrier between ferromagnets and semiconductors that resulted from the mismatch in the electrical conductivities.[40] The BCP and MoO_3 layers blocked the injection of holes and electrons from the top Al electrode, respectively, and thus, only the spin-polarized current injected from the bottom Ni electrode was measured. We obtained *I*–*V* curves 10 times using a CISS device with an active area size of 10 mm^2 to ensure the measurement reliability. This procedure was iterated with the Ni layer magnetized along the opposite direction. As shown in Figure 2e, the current magnitudes of the *R*-NEA-based CISS devices at 3 V were 5.02 and 0.73 mA when the Ni electrode was magnetized up and down, respectively.

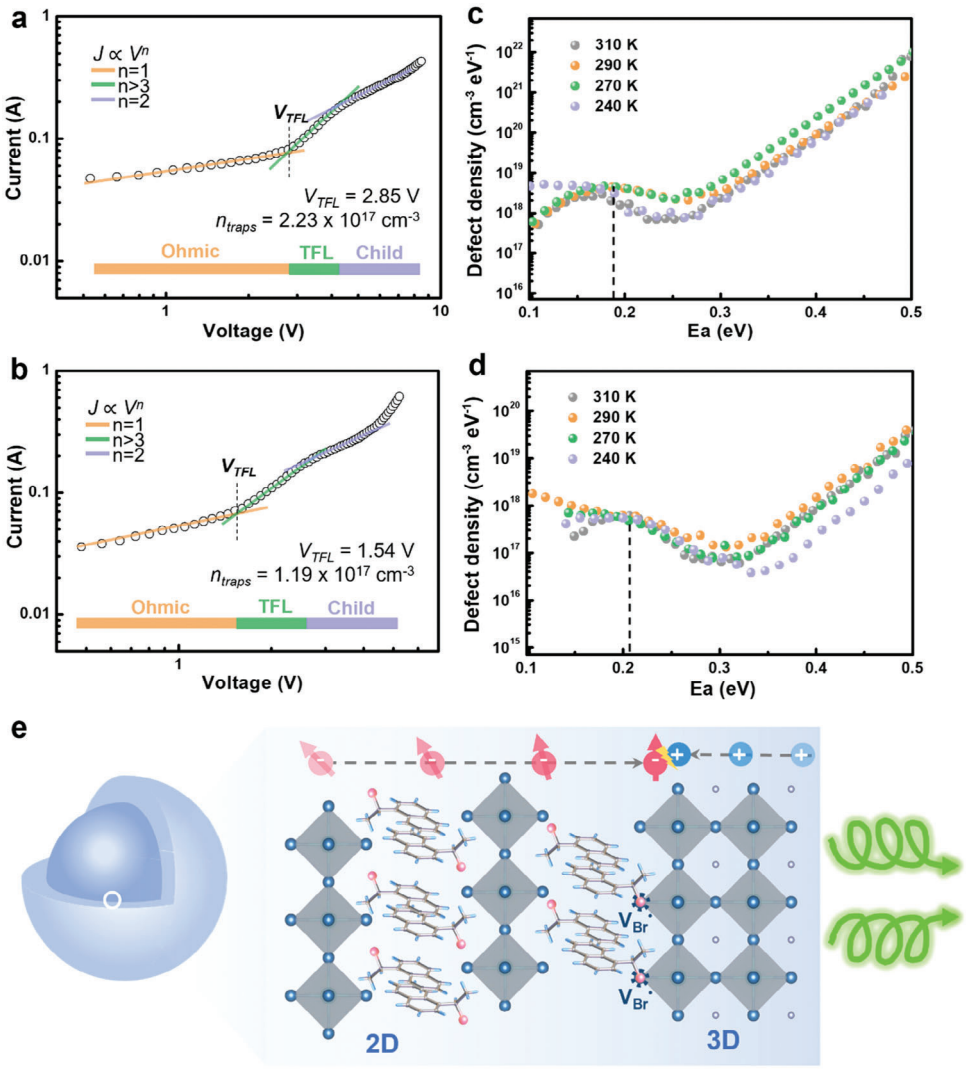

Figure 3. Current–voltage (*I–V*) curves of devices with the ITO/perovskite QDs/Au configuration, fabricated with a) $CsPbBr_3$ core QDs and b) core–shell QDs with *R*-NEA-based shell. The curves were obtained in dark conditions using the SCLC method. Defect density distributions derived from TAS measurements. The maximum peaks located at energy levels of 0.19 and 0.21 eV indicate the defect density of perovskite QDs c) without and d) with a shell composed of 2D chiral OIHPs, respectively. e) Schematic of the mechanism of the spin-polarized charge injection as well as bromine vacancy healing by the introduction of 2D chiral shells.

By contrast, the current magnitudes of the *S*-NEA-based CISS devices were 0.53 and 3.45 mA at 3 V when the Ni electrode was magnetized up and down, respectively (Figure 2f). Using these measurements, P_{spin} was calculated to be +74.6% and −73.4% at 3 V for the *R*- and *S*-NEA-based core–shell QD films, respectively. The P_{spin} values obtained from the CISS measurements were consistent with those derived through the mCP-AFM analysis. The CISS devices fabricated with the *rac*-NEA-based core–shell QD films exhibited almost identical *I–V* characteristics regardless of the magnetization direction of the Ni layer (Figure S15, Supporting Information). Therefore, it could be concluded that the spin state of the injected charge carriers is effectively biased according to the handedness of the NEA-based 2D chiral shells.

To clarify the mechanism of luminescence property enhancement after the deposition of the NEA chiral shell (Figure 2a), we examined the electronically active defects, because the recombination of the injected charge carriers strongly depends on the concentrations and energy levels of the defects. The trap density of the perovskite QDs before and after 2D chiral shell formation was evaluated through a space-charge-limited current (SCLC) analysis.[41–43] To this end, devices with a configuration of glass/ITO/perovskite QD/Au were fabricated, and their *I–V* curves were measured in dark conditions. As shown in **Figure 3**a,b, the *I–V* curves exhibited three regions: Ohmic, trap-filled, and Child regions. At low voltages (i.e., the Ohmic region), the current increased linearly with the voltage owing to an Ohmic response. At intermediate voltages (i.e., trap-filled limit region, TFL), the current rapidly increased in an exponential manner, which indicated that all the available trap states were filled by the injected carriers. The voltage between the Ohmic and trap-filled regimes, i.e., the trap-filled limit voltage (V_{TFL}) depended on the

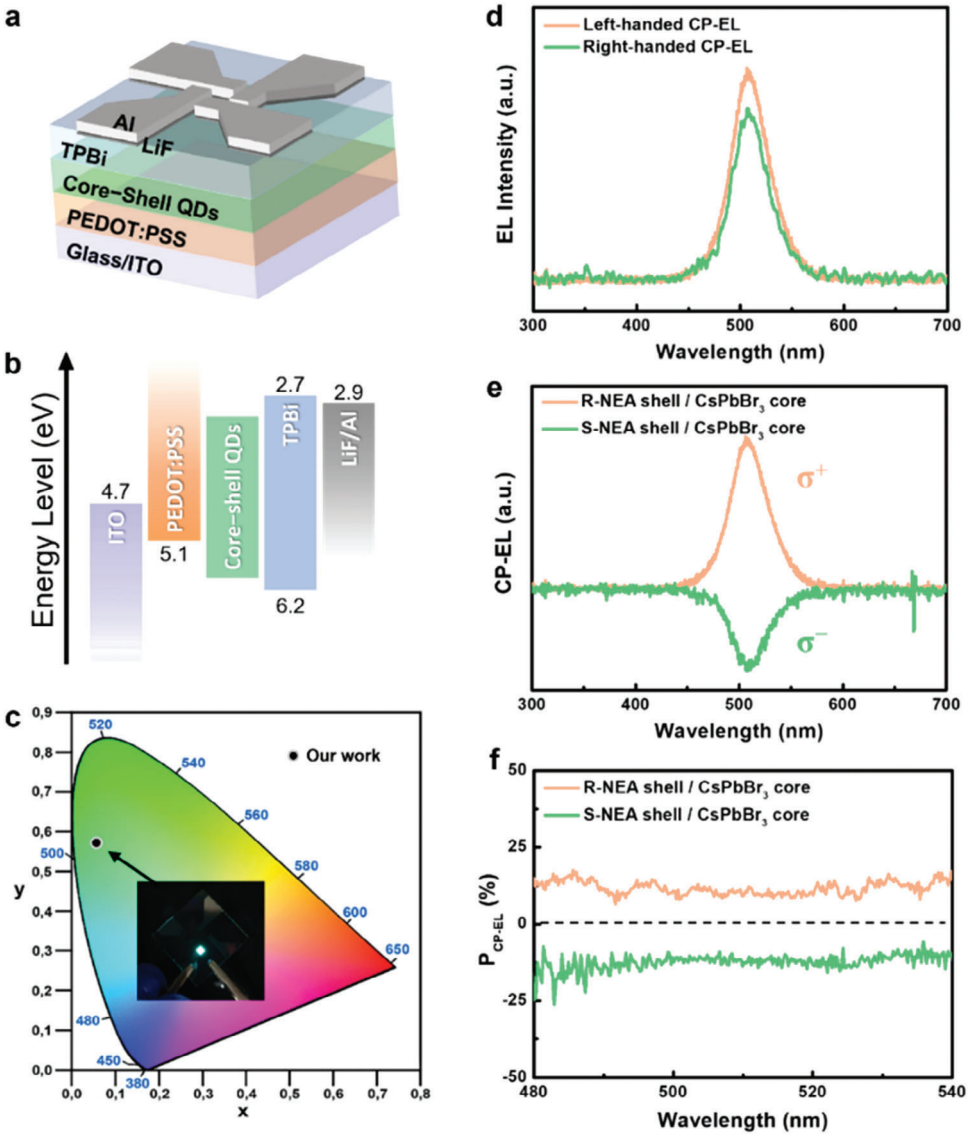

Figure 4. a) Device configuration and b) band energy diagram of the prepared spin-LEDs. c) CIE 1931 chromatic coordinates of emitted green light. The inset presents digital photo of the operating spin-LEDs. d) Left- and right-handed CP-EL spectra of spin-LEDs based on core–shell chiral QDs with an *R*-NEA 2D chiral shell. e) CP-EL spectra and f) polarization degree of EL ($P_{CP\text{-}EL}$) of the spin-LEDs based on $CsPbBr_3$ QDs with the *R*-NEA 2D chiral shell.

density of the trap states. Thus, the trap density (n_{trap}) was calculated as[41–43]

$$V_{TFL} = \frac{en_{trap}L^2}{2\varepsilon\varepsilon_0} \quad (3)$$

where L is the film thickness, ϵ is the permittivity of the perovskite film, and ϵ_0 is the vacuum permittivity. The V_{TFL} values associated with the $CsPbBr_3$ QDs films without and with the NEA shell were 2.85 and 1.54 V, respectively, with the corresponding n_{trap} being 2.23×10^{17} and 1.19×10^{17} cm^{-3}, respectively. The obtained n_{trap} values were highly consistent with the reported defect density of $CsPbBr_3$ perovskite QDs.[44,45] The 46% reduction in the trap density after the formation of the NEA-based chiral shell indicated that the NEA 2D cation successfully passivates the defects of the $CsPbBr_3$ core. Also, it should be noted that the small satellite peaks next to each Pb 4f core level signal corresponding to the metallic lead (Pb^0) are eliminated after the injection of shell precursor in the previously mentioned Pb 4f XPS spectra (Figure S5a, Supporting Information). This observation is explained by the effective passivation of uncoordinated Pb^{2+} by the chiral organic cations after the deposition of 2D chiral shell.

To further confirm the passivation effect of the NEA shells on the surface of the $CsPbBr_3$ QDs, we performed a temperature-dependent admittance spectroscopy (TAS) analysis, which is an effective tool for evaluating the defect density and energy level.[46–48] The sample devices had a configuration of ITO/PEDOT:PSS/perovskite QDs/2,2′,2″-(1,3,5-benzinetriyl)-tris(1-phenyl-1-*H*-benzimidazole) (TPBi)/lithium fluoride (LiF)/Al. The capacitance spectra were obtained in dark

conditions with a temperature range of 240–310 K and frequency ranging between 0.3 MHz and 100 Hz. The energy level of the defects, E_a, was calculated as

$$\omega_o(T) = \xi_o T_2 \exp(-E_a/kT) \quad (4)$$

where ω_o is the characteristic transition frequency corresponding to the minima in the $\omega dC/d\omega$ versus ω graph, C is the capacitance, ω is the applied frequency, ξ_o is the temperature-independent parameter, k is the Boltzmann constant, and T is the absolute temperature. In the plot of $\ln(\omega_o/T_2)$ versus $1/T$, E_a can be determined as the slope of the linear regression line. Figure S16 (Supporting Information) shows the defect energy level of $CsPbBr_3$ QDs with or without the 2D chiral perovskite shell based on the NEA cation. Both samples exhibited similar defect energy levels (0.19–0.21 eV) that were above the valence band maximum. The origin of such shallow defects could be attributed to the role of bromine ion vacancies as nonradiative recombination centers. According to a previous report on $CsPbBr_3$ QDs, bromine vacancies (i.e., $V_{Br}^{\bullet}$) are mainly located at the surface of the QDs.[49] The defect density, N_T, can be derived by the following equation:

$$N_T = -\frac{V_{bi}}{qW}\frac{dC}{d\omega}\frac{\omega}{kT} \quad (5)$$

where V_{bi} is the built-in potential, q is an elementary charge, and W is the depletion width. The values of V_{bi} and W were obtained from a Mott–Schottky analysis (Figure S17, Supporting Information). The defect density distribution in the QDs exhibited a broad spectrum with the maxima located at the defect energy level of 0.19–0.21 eV regardless of the presence of the chiral shell (Figure 3c,d). The defect density values obtained from the TAS measurement were 4.60×10^{18} and 6.23×10^{17} cm^{-3} eV^{-1} for the $CsPbBr_3$ QDs without and with the NEA-based chiral shell, respectively. These results suggested that the $CsPbBr_3$ QDs with the NEA chiral shell had an explicitly lower defect density compared to those without the shell. According to previous studies on the defect density in 2D/3D heterostructured perovskite, the defects in perovskite materials mainly consist of halide ion vacancies that can be effectively passivated by introducing bulky 2D cations.[50–53] Most of the 2D spacer cations are Lewis bases (i.e., electron donors) containing an ammonium functional group that can bond with and/or passivate halide ion vacancies by van der Waals interactions (Figure 3e). Hence, the enhanced luminescence of the core–shell QDs likely originated from the defect passivation effect by 2D chiral organic cations, which reduced nonradiative recombination. These findings highlight that the formation of the NEA-based chiral shell enhances not only the chiroptical property of core–shell QDs compared with the MBA counterpart but also the brightness of inorganic perovskite QDs.

Considering the outstanding chiroptical and electrical properties of the NEA-based core–shell chiral QDs, we fabricated spin-LEDs with the configuration of glass/ITO/PEDOT:PSS/chiral QDs with NEA shell/TPBi/LiF/Al (**Figure 4a**). Figure 4b schematically illustrates the band energy diagram of the fabricated spin-LEDs. After the injection of electrons and holes from the top Al and bottom ITO electrode, respectively, the TPBi layer transferred the electrons while blocking the holes, whereas the PEDOT:PSS layer transferred the holes and blocked the electrons. In this manner, the injected charge carriers reach 2D chiral shell and their spin state is biased during transportation owing to the chiral-induced spin selectivity effect. Then, they funnel into the $CsPbBr_3$ emissive core with their spin aligned and then radiatively recombine, generating CPL. As demonstrated in Figure 4c, the fabricated spin-LEDs exhibited green emission with Commission Internationale de l'Eclairage (CIE) coordinates of (0.067, 0.589). The digital photograph of the operating spin-LEDs is presented in the inset of Figure 4c. The fabricated spin-LEDs exhibited a turn-on voltage of 2.2 V and maximum EQE of 5.47% (Figure S18, Supporting Information), which is higher than those of the previous works (Table S2, Supporting Information).[21,54] The detailed performance parameters of spin-LEDs are summarized in **Table 1**. The operational stability of the spin-LEDs was also assessed by tracking luminance decay under the constant current density at peak EQE, as illustrated in Figure S19 (Supporting Information). It is important to emphasize that the spin-LEDs fabricated with core–shell QDs exhibited a half-lifetime (referred to as T_{50}, the time when luminance diminishes to 50% of its initial value) of ≈8.3 min. This result is highly comparable to those of previously reported perovskite-based green LEDs. The performance of the device prepared with 2D shell based on achiral ligands (i.e., *rac*-NEA) as well as the QDs without shells was also investigated. As demonstrated in Figure S20 (Supporting Information), the EQE of the devices prepared with core–shell QDs with *rac*-NEA exhibited almost similar EQE value of 5.13% with that of the device based on *R*-NEA-based core–shell QDs. Meanwhile, the EQE of LEDs fabricated with $CsPbBr_3$ core QDs was found to be slightly higher (6.51%). Higher EQE value likely results from the absence of 2D chiral shell with the low electrical conductivity. The CP-EL was measured by sequentially transmitting the emitted light into a $\lambda/4$ plate and linear polarizer system and a spectrometer and then separating it into left and right components. Since $CsPbBr_3$ QDs with *R*- and *S*-NEA 2D chiral shells would exhibit CP-EL with opposite handedness, it was represented as positive/negative EL (Figure 4e). The CP-EL polarization degree, $P_{CP\text{-}EL}$, was calculated as

$$P_{CP-EL} = \frac{I_{left} - I_{right}}{I_{left} + I_{right}} \times 100\% \quad (6)$$

where I_{left} and I_{right} are the EL intensities of the left- and right-CP light, respectively. Spin-LEDs based on the $CsPbBr_3$ QDs with the NEA shell showed distinct CP-EL spectra centered at 506 nm with the average $P_{CP\text{-}EL}$ of ±12% at $480 \leq \lambda \leq 540$ nm (Figure 4e,f). The high $P_{CP\text{-}EL}$ indicates that the core–shell structure can generate electroluminescence with a high polarization degree. In general, a core–shell configuration with a well-defined interface decreases the diffusion length of the injected carriers after they pass the CISS layer, while minimizing the spin scattering, especially at

Table 1. Performance parameters of the spin-LED fabricated with NEA-based core–shell QDs..

Device type	V_{ON} [V]	EL peak [nm]	Max luminance [cd m^{-2}]	EQE [%]	CIE
NEA-based core–shell QDs	2.2	505	1962	5.47	(0.067, 0.589)

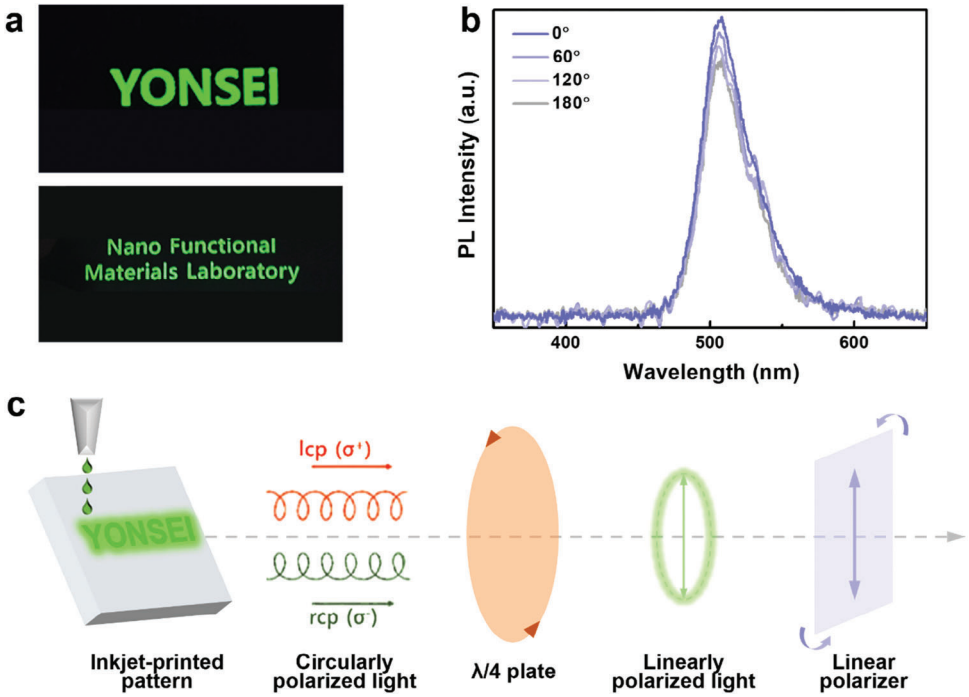

Figure 5. a) Digital photograph of inkjet-printed green-emitting core–shell QDs with patterns of "YONSEI" (lighting area, 30 × 8 mm^2) and "Nano Functional Materials Laboratory" (lighting area, 40 × 9 mm^2) on soda lime glass under UV irradiation. b) PL spectra of the inkjet-printed YONSEI pattern with varying rotational degrees of the linear polarizer, collected with the spectrometer under UV irradiation. c) Schematic of the process of detection of circularly polarized light emitted from inkjet-printed core–shell QDs.

room temperature, at which the spin-dephasing time is substantially limited. By contrast, the spin-LEDs prepared with *rac*-NEA-based core–shell QDs did not emit any CP-EL (Figure S21, Supporting Information). With the consideration of negligible CP-EL intensity of spin-LEDs based on *rac*-NEA chiral shell, it can be deduced that the resulting CP-EL spectra were rarely affected by optical interference or instrumental errors.

To satisfy the requirements for the potential application of spin-LEDs as a next-generation display, we examined its compatibility with inkjet printing, which is one of the most broadly adapted technologies for upscaling perovskite-based optoelectronic devices. For stable formation and ejection of droplets from nozzles, the core–shell QDs were redispersed into highly viscous 1-octadecene (details of the inkjet printing process can be found in the Experimental Section). Using the ink of the core–shell QDs with the *R*-NEA 2D chiral shell, the target patterns were successfully printed with high uniformity, as demonstrated in **Figure 5a**. Microscopic fluorescence images of patterned inkjet-printed core–shell QD arrays are also demonstrated in Figure S22 (Supporting Information).

The PL spectra of the inkjet-printed QD thin films subjected to ultraviolet (UV) irradiation were acquired using the fluorescence spectrophotometer (Figure 5b). The PL emission peaks of the inkjet-printed patterns were located at ≈508 nm, consistent with the PL spectra of the as-prepared core–shell QD dispersions. Furthermore, during the measurement of PL spectra, we placed a broadband $\lambda/4$ waveplate and linear polarizer between the patterned core–shell QD films and spectrometer to quantitatively identify the polarized emission induced by the CISS effect through the 2D chiral OIHP shell. The CPL generated from the patterned core–shell QDs was converted to linearly polarized light whose intensity could be controlled by the linear polarizer (Figure 5c). Notably, the PL intensities of the patterned core–shell QD decreased (the PL peak intensities decreased by ≈15%) as the rotational angle increased from 0° to 180°. These results demonstrated that the synthesized core–shell QDs successfully generated PL with high circular polarization owing to the efficient carrier spin polarization capability. The change in the PL intensity according to the rotational angle of the linear polarizer could be visually observed (Video S1, Supporting Information). The CPL spectrum of core–shell QD films was also collected at room temperature, as demonstrated in Figure S23 (Supporting Information). The core–shell QD films based on *S*-NEA chiral shell clearly exhibited strong CPL peak with negative sign. Based on these results, we can conclude that the proposed NEA-based core–shell QDs can serve as next-generation display with circularly polarized emission capabilities.

3. Conclusions

This paper describes the fabrication of room-temperature spin-LEDs based on core–shell heterostructured perovskite QDs. Achiral $CsPbBr_3$ inorganic QDs prepared by the hot-injection method were used as the emissive core. The shell consisted of 2D chiral OIHPs, in which population of the spin-controlled charge carriers was increased according to the handedness of the chiral organic cation. The use of inorganic QDs promoted the formation of heterostructured perovskite QDs with a discrete boundary

between the core and shell, which helped achieve outstanding luminescence and spin filtering effect. Moreover, we introduced a *R*-/*S*-NEA 2D chiral cation with high MTDM in the shell layer surrounding the QDs. These cations exhibited a superior chiroptical property compared with those of the conventional *R*-/*S*-MBA counterpart. The strong spin polarization property of the core–shell QDs was confirmed by performing mCP-AFM and CISS device measurements. The *R*-/*S*-NEA organic cation enhanced the luminescence property of heterostructured QDs, increasing the PLQY from 71% (core QDs) to 78% (core–shell QDs). This enhanced quantum yield originated from the defect passivation by the 2D chiral cation (i.e., *R*-/*S*-NEA), as confirmed by quantitative defect analyses based on TAS and SCLC. The spin-LEDs fabricated with the core–shell heterostructured QDs exhibited a maximum EQE of 5.47% and CP-EL with a $P_{CP\text{-}EL}$ of over 12% at room temperature. Finally, core–shell QD inks were formulated for inkjet printing to fabricate various patterns. The printed patterns exhibited strong CPL that could be detected even with the naked eye. This research provides the basis for the potential application of perovskite-based spin-LEDs with high spin polarization for next-generation displays.

4. Experimental Section

Materials: Cesium carbonate (Cs_2CO_3, 99.9%), lead bromide ($PbBr_2$, 99.999%, trace metal basis), DMF (anhydrous, 99.8%), 1-octadecene (1-ODE, 90%), ethanol (anhydrous, ≥99.5%), toluene (anhydrous, 99.8%), *n*-hexane (anhydrous, 95%), oleic acid (OAc, 90%), oleylamine (OA, 70%, technical grade), *R*-/*S*-MBA (98%), *R*-/*S*-NEA (98%), TPBi, LiF (≥99.5%, trace metal basis), BCP (99.99%, trace metal basis), and hydrobromic acid (HBr, ACS reagent, 48%) were purchased from Merk (Darmstadt, Germany). Formamidinium bromide was purchased from GreatCell solar (Queanbeyan, Australia). PEDOT:PSS (HTL solar 3) was purchased from Ossila (Sheffield, UK). All chemicals were used as-received, without any modification.

Synthesis of Chiral Organic Ammonium Halide Salts: 1.2 mmol of chiral organic amine (*R*-/*S*-MBA and *R*-/*S*-NEA) and 1.3 mmol of HBr were mixed in 0.5 mL ethanol. After vigorous stirring for over 12 h, the solution was fully dried at 80 °C under vacuum, yielding *R*-/*S*-MBABr and *R*-/*S*-NEABr chiral organic ammonium salts.

Fabrication of the Core–Shell QDs: To prepare the Cs-oleate stock solution, 0.815 g of Cs_2CO_3 was loaded into a 100 mL 3-neck flask along with 40 mL of 1-ODE and 2.5 mL oleic acid. This flask was degassed for 1 h at 100 °C under vacuum and then heated in a N_2 atmosphere to 120 °C until the Cs_2CO_3 was fully dissolved. In a 25 mL three-necked flask, 55 mg of $PbBr_2$ was suspended in 5 mL ODE, heated to 100 °C, and then degassed under vacuum for 30 min. Subsequently, the reaction mixture was heated to 110 °C in a N_2 atmosphere, followed by the addition of 0.5 mL OA and 0.5 mL OAc. Once the $PbBr_2$ was fully dissolved, the solution was heated to 180 °C. At this point, 0.8 mL of cesium oleate solution, which was pre-heated at ≈100 °C was swiftly injected into the $PbBr_2$ solution, allowed to react for 15 s, and then quenched with a water–ice bath. The as-prepared solution was centrifuged at 12 000 rpm for 5 min (Combi 541R, Hanil Scientific Inc., Gimpo, South Korea), and the supernatant was discarded. The precipitate was redispersed in 0.5 mL hexane and then subjected to an identical centrifugation step (12 000 rpm, 5 min). The obtained solution was diluted with 10 mL toluene and used for shell formation. The $FAPbBr_3$ QDs were synthesized by following a previously reported ligand-assisted reprecipitation method and then redispersed in toluene for the shell formation.[25] To prepare the shell precursor, 0.2 mmol of *R*-/*S*-/*rac*-MBABr or *R*-/*S*-/*rac*-NEABr and 0.1 mmol of $PbBr_2$ were dissolved in 1 mL DMF, followed by the syringe-based addition of 200 µL OAc and 40 µL OA. Afterward, the shell precursor was swiftly injected into the core QD (i.e., either $CsPbBr_3$ or $FAPbBr_3$) dispersions with designated molar concentrations. After the injection of the shell precursor, the resulting core–shell QD dispersions were purified by centrifuging at 12 000 rpm for 5 min and redispersed in toluene.

Fabrication and Characterization of the Spin-LEDs: 180 nm ITO patterned glass samples were cleaned by sequential sonication in deionized water, acetone, and 2-propanol for 15 min each, followed by ultraviolet–ozone (UVO) treatment for 15 min. After UVO treatment, the PEDOT:PSS hole injection layer was spin-coated at 4000 rpm for 40 s in ambient conditions and then annealed at 130 °C for 30 min. After the deposition of the hole injection layer, core–shell QD solutions with varying compositions were spin-coated at 3000 rpm for 30 s and then annealed at 70 °C for 3 min. The samples were transferred to a thermal evaporator, and then, 45 nm thick TPBi, 1 nm thick LiF, and 100 nm thick Al electrodes were sequentially evaporated with deposition speeds of 0.5, 0.05, and 1 Å s^{-1}, respectively. The luminance (*L*) and EL characteristics of the spin-LEDs were measured using a spectroradiometer (CS 2000, Konica Minolta, Tokyo, Japan). To detect CP-EL, a broadband $\lambda/4$ waveplate and linear polarizer were placed between the spin-LEDs and spectrometer.[20] Left-/right-handed CP-EL was measured through 90° rotation of the linear polarizer. The device EQE was calculated from the *L*, current density (*J*), and EL spectra by assuming a Lambertian emission profile.

Characterization of the Chiroptical, Structural, and Optoelectronic Properties: CD and absorbance spectra were obtained with a CD spectrometer (J-815, JASCO, Tokyo, Japan). Steady-state PL spectra of the core–shell QD colloidal dispersions were collected with an excitation beam wavelength of 350 nm (FluoroMax Plus, Horiba, Kyoto, Japan). The CPL spectrum was measured using CPL spectrometer (CPL-300, JASCO, Tokyo, Japan) with a scan rate of 100 nm min^{-1} and a pitch of 0.2 nm under 350 nm laser excitation. The surface and cross-sectional structures of the samples were acquired with field-emission scanning electron microscopy (JSM-IT500, JEOL Ltd., Tokyo, Japan). The crystal structure of the QD films was determined using an XRD diffractometer (Rigaku Miniflex 600, The Woodlands, USA). SCLC measurements of the spin-LEDs were obtained using a Keithley 2400 source measurement unit (Keithley Instruments Inc., Cleveland, OH, USA) in dark conditions. TEM images were obtained using a double Cs and monochromated HRTEM unit (JEM-ARM200F NEOARM, JEOL Ltd., Tokyo, Japan) with an accelerating voltage of 200 kV. The TAS spectra were recorded using a frequency response analyzer (SI 1287, Solartron, Leicester, UK) with a perturbation of 30 mV AC and frequency sweep from 0.3 MHz to 1 kHz in short-circuit and dark conditions. To control the temperature of the devices, a temperature-controlling stage combined with a liquid nitrogen cooling system (LNP95, Linkam Scientific, Salfords, UK) was used.

Characterization of the Spin Polarization Properties: mCP-AFM measurements were conducted using an AFM system (SPA 400, Seiko Instruments, Inc., Chiba, Japan) in ambient conditions. Co–Cr-coated MFMR-10 tips with a force constant of 2.8 N m^{-1} (NanoWorld, Neuchâtel, Switzerland) were used. The measurement was conducted after the pre-magnetization of the Co–Cr-coated tips by a permanent magnet for more than 60 min. The *I*–*V* curves of devices with the configuration of ITO/PEDOT:PSS/core–shell QD thin films were measured by sweeping the voltage from −2 to +2, resulting in 1024 datapoints. Moreover, the *I*–*V* curves were repeatedly measured from 30 positions for each sample. To confirm the results obtained by the mCP-AFM, CISS devices with a large active area were manufactured according to the following procedure. A 50 nm thick ferromagnetic Ni layer was thermally evaporated on soda lime glass with a deposition speed of 0.5 Å s^{-1}. Subsequently, an Al_2O_3 layer with a thickness of 1.5 nm was deposited by atomic layer deposition. The core–shell structured QDs with the *R*-/*S*-NEA 2D chiral shell were spin-coated at 3000 rpm for 30 s onto the Al_2O_3 layer, followed by thermal evaporation of 50 nm thick BCP, 15 nm thick MoO_3, and 100 nm thick Al layers, with deposition speeds of 0.5, 0.1, and 1 Å s^{-1}, respectively. The *I*–*V* characteristics of the prepared CISS devices were measured using a Keithley 2400 unit (Keithley Instruments Inc., Cleveland, OH, USA) with the sweeping voltage ranging from −3 to +3 V in dark conditions.

Inkjet Printing: Various patterns were inkjet printed using the Dimatix DMP-2850 device (Fujifilm, Tokyo, Japan). The cartridge was a Dimatix

DMC-11610 with a nozzle size of 21.54 µm, which generated ≈10 pL droplets. The jetting velocity was 3 m s^{-1}, and the jetting frequency was 1 kHz with a driving voltage of 30–33 V. The temperature of both the substrate and nozzle was maintained at 25 °C to ensure the stable ejection of droplets. Subsequently, the inkjet-printed QD patterns were annealed at 70 °C for 10 min.

Supporting Information

Supporting Information is available from the Wiley Online Library or from the author.

Acknowledgements

This research was supported by the National R&D Program through the National Research Foundation of Korea (NRF) funded by the Ministry of Science and ICT (Grant Nos. 2021R1A3B1068920 and 2021M3H4A1A03049662). This research was also supported by the Yonsei Signature Research Cluster Program of 2021 (Grant No. 2021-22-0002).

Conflict of Interest

The authors declare no conflict of interest.

Data Availability Statement

The data that support the findings of this study are available from the corresponding author upon reasonable request.

Keywords

chiral-induced spin selectivity, core–shell, nanocrystals, perovskite, spin-LEDs

Received: September 11, 2023
Revised: November 9, 2023
Published online: December 5, 2023

[1] A. Hirohata, K. Takanashi, *J. Phys. D: Appl. Phys.* **2014**, *47*, 193001.
[2] N. Nishizawa, H. Munekata, *Micromachines* **2021**, *12*, 573.
[3] E. Togan, Y. Chu, A. S. Trifonov, L. Jiang, J. Maze, L. Childress, M. V. G. Dutt, A. S. Sørensen, P. R. Hemmer, A. S. Zibrov, M. D. Lukin, *Nature* **2010**, *466*, 730.
[4] D. Yang, P. Duan, L. Zhang, M. Liu, *Nat. Commun.* **2017**, *8*, 15727.
[5] S. A. Wolf, D. D. Awschalom, R. A. Buhrman, J. M. Daughton, S. von Molnár, M. L. Roukes, A. Y. Chtchelkanova, D. M. Treger, *Science* **2001**, *294*, 1488.
[6] F. Pulizzi, *Nat. Mater.* **2012**, *11*, 367.
[7] R. Naaman, Y. Paltiel, D. H. Waldeck, *J. Phys. Chem. Lett.* **2020**, *11*, 3660.
[8] R. Naaman, D. H. Waldeck, *J. Phys. Chem. Lett.* **2012**, *3*, 2178.
[9] J. Ahn, E. Lee, J. Tan, W. Yang, B. Kim, J. Moon, *Mater. Horiz.* **2017**, *4*, 851.
[10] P. Odenthal, W. Talmadge, N. Gundlach, R. Wang, C. Zhang, D. Sun, Z.-G. Yu, Z. Valy Vardeny, Y. S. Li, *Nat. Phys.* **2017**, *13*, 894.
[11] C. Yuan, X. Li, S. Semin, Y. Feng, T. Rasing, J. Xu, *Nano Lett.* **2018**, *18*, 5411.
[12] Y. Dong, Y. Zhang, X. Li, Y. Feng, H. Zhang, J. Xu, *Small* **2019**, *15*, 1902237.
[13] G. Long, C. Jiang, R. Sabatini, Z. Yang, M. Wei, L. N. Quan, Q. Liang, A. Rasmita, M. Askerka, G. Walters, X. Gong, J. Xing, X. Wen, R. Quintero-Bermudez, H. Yuan, G. Xing, X. R. Wang, D. Song, O. Voznyy, M. Zhang, S. Hoogland, W. Gao, Q. Xiong, E. H. Sargent, *Nat. Photonics* **2018**, *12*, 528.
[14] H. Lu, C. Xiao, R. Song, T. Li, A. E. Maughan, A. Levin, R. Brunecky, J. J. Berry, D. B. Mitzi, V. Blum, M. C. Beard, *J. Am. Chem. Soc.* **2020**, *142*, 13030.
[15] C. Zhang, D. Sun, C. X. Sheng, Y. X. Zhai, K. Mielczarek, A. Zakhidov, Z. V. Vardeny, *Nat. Phys.* **2015**, *11*, 428.
[16] M. Isarov, L. Z. Tan, M. I. Bodnarchuk, M. V. Kovalenko, A. M. Rappe, E. Lifshitz, *Nano Lett.* **2017**, *17*, 5020.
[17] G. Xing, N. Mathews, S. Sun, S. S. Lim, Y. M. Lam, M. Grätzel, S. Mhaisalkar, T. C. Sum, *Science* **2013**, *342*, 344.
[18] J. Crassous, M. J. Fuchter, D. E. Freedman, N. A. Kotov, J. Moon, M. C. Beard, S. Feldmann, *Nat. Rev. Mater.* **2023**, *8*, 365.
[19] L. Mao, C. C. Stoumpos, M. G. Kanatzidis, *J. Am. Chem. Soc.* **2019**, *141*, 1171.
[20] Y.-H. Kim, Y. Zhai, H. Lu, X. Pan, C. Xiao, E. A. Gaulding, S. P. Harvey, J. J. Berry, Z. V. Vardeny, J. M. Luther, M. C. Beard, *Science* **2021**, *371*, 1129.
[21] C. Ye, J. Jiang, S. Zou, W. Mi, Y. Xiao, *J. Am. Chem. Soc.* **2022**, *144*, 9707.
[22] Y. Wang, T. Zhang, M. Kan, Y. Li, T. Wang, Y. Zhao, *Joule* **2018**, *2*, 2065.
[23] J. Ahn, S. Ma, J.-Y. Kim, J. Kyhm, W. Yang, J. A. Lim, N. A. Kotov, J. Moon, *J. Am. Chem. Soc.* **2020**, *142*, 4206.
[24] M. I. Bodnarchuk, S. C. Boehme, S. ten Brinck, C. Bernasconi, Y. Shynkarenko, F. Krieg, R. Widmer, B. Aeschlimann, D. Günther, M. V. Kovalenko, I. Infante, *ACS Energy Lett.* **2019**, *4*, 63.
[25] I. Levchuk, A. Osvet, X. Tang, M. Brandl, J. D. Perea, F. Hoegl, G. J. Matt, R. Hock, M. Batentschuk, C. J. Brabec, *Nano Lett.* **2017**, *17*, 2765.
[26] Y. Liu, B. J. Kim, H. Wu, G. Boschloo, E. M. J. Johansson, *ACS Appl. Energy Mater.* **2021**, *4*, 9276.
[27] H. Xu, Z. Liang, J. Ye, S. Xu, Z. Wang, L. Zhu, X. Chen, Z. Xiao, X. Pan, G. Liu, *Chem. Eng. J.* **2022**, *437*, 135181.
[28] S. Ma, Y.-K. Jung, J. Ahn, J. Kyhm, J. Tan, H. Lee, G. Jang, C. U. Lee, A. Walsh, J. Moon, *Nat. Commun.* **2022**, *13*, 3259.
[29] J. Xing, Y. Zhao, M. Askerka, L. N. Quan, X. Gong, W. Zhao, J. Zhao, H. Tan, G. Long, L. Gao, Z. Yang, O. Voznyy, J. Tang, Z.-H. Lu, Q. Xiong, E. H. Sargent, *Nat. Commun.* **2018**, *9*, 3541.
[30] K. Zhong, S. Lu, W. Guo, J. Su, S. Sun, J. Hai, F. Chen, A. Wang, B. Wang, *J. Mater. Chem. A* **2021**, *9*, 10180.
[31] Z. Wang, R. Fu, F. Li, H. Xie, P. He, Q. Sha, Z. Tang, N. Wang, H. Zhong, *Adv. Funct. Mater.* **2021**, *31*, 2010009.
[32] S. Bhaumik, S. A. Veldhuis, Y. F. Ng, M. Li, S. K. Muduli, T. C. Sum, B. Damodaran, S. Mhaisalkar, N. Mathews, *Chem. Commun.* **2016**, *52*, 7118.
[33] W. Chen, S. Bhaumik, S. A. Veldhuis, G. Xing, Q. Xu, M. Grätzel, S. Mhaisalkar, N. Mathews, T. C. Sum, *Nat. Commun.* **2017**, *8*, 15198.
[34] M. I. Saleem, S. Yang, R. Zhi, M. Sulaman, P. V. Chandrasekar, Y. Jiang, Y. Tang, A. Batool, B. Zou, *Adv. Mater. Interfaces* **2020**, *7*, 2000360.
[35] X. Tang, J. Yang, S. Li, Z. Liu, Z. Hu, J. Hao, J. Du, Y. Leng, H. Qin, X. Lin, Y. Lin, Y. Tian, M. Zhou, Q. Xiong, *Adv. Sci.* **2019**, *6*, 1900412.
[36] Z. Shi, Y. Li, S. Li, X. Li, D. Wu, T. Xu, Y. Tian, Y. Chen, Y. Zhang, B. Zhang, C. Shan, G. Du, *Adv. Funct. Mater.* **2018**, *28*, 1707031.
[37] X. Tong, X.-T. Kong, Y. Zhou, F. Navarro-Pardo, G. S. Selopal, S. Sun, A. O. Govorov, H. Zhao, Z. M. Wang, F. Rosei, *Adv. Energy Mater.* **2018**, *8*, 1701432.
[38] J. Son, S. Ma, Y.-K. Jung, J. Tan, G. Jang, H. Lee, C. U. Lee, J. Lee, S. Moon, W. Jeong, A. Walsh, J. Moon, *Nat. Commun.* **2023**, *14*, 3124.

[39] M. K. Jana, R. Song, H. Liu, D. R. Khanal, S. M. Janke, R. Zhao, C. Liu, Z. Valy Vardeny, V. Blum, D. B. Mitzi, *Nat. Commun.* **2020**, *11*, 4699.
[40] E. I. Rashba, *Phys. Rev. B* **2000**, *62*, R16267.
[41] R. H. Bube, *J. Appl. Phys.* **1962**, *33*, 1733.
[42] D. Shi, V. Adinolfi, R. Comin, M. Yuan, E. Alarousu, A. Buin, Y. Chen, S. Hoogland, A. Rothenberger, K. Katsiev, Y. Losovyj, X. Zhang, P. A. Dowben, O. F. Mohammed, E. H. Sargent, O. M. Bakr, *Science* **2015**, *347*, 519.
[43] Z. Liu, J. Hu, H. Jiao, L. Li, G. Zheng, Y. Chen, Y. Huang, Q. Zhang, C. Shen, Q. Chen, H. Zhou, *Adv. Mater.* **2017**, *29*, 1606774.
[44] H. Zhu, G. Tong, J. Li, E. Xu, X. Tao, Y. Sheng, J. Tang, Y. Jiang, *Adv. Mater.* **2022**, *34*, 2205092.
[45] Y. Gao, Y. Liu, F. Zhang, X. Bao, Z. Xu, X. Bai, M. Lu, Y. Wu, Z. Wu, Y. Zhang, Q. Wang, X. Gao, Y. Wang, Z. Shi, J. Hu, W. W. Yu, Y. Zhang, *Adv. Mater.* **2022**, *34*, 2207445.
[46] T. Walter, R. Herberholz, C. Müller, H. W. Schock, *J. Appl. Phys.* **1996**, *80*, 4411.
[47] H.-S. Duan, H. Zhou, Q. Chen, P. Sun, S. Luo, T.-B. Song, B. Bob, Y. Yang, *Phys. Chem. Chem. Phys.* **2015**, *17*, 112.
[48] J. H. Heo, D. H. Song, H. J. Han, S. Y. Kim, J. H. Kim, D. Kim, H. W. Shin, T. K. Ahn, C. Wolf, T.-W. Lee, S. H. Im, *Adv. Mater.* **2015**, *27*, 3424.
[49] M. H. Du, *J. Mater. Chem. A* **2014**, *2*, 9091.
[50] H. Uratani, K. Yamashita, *J. Phys. Chem. Lett.* **2017**, *8*, 742.
[51] Y. Bai, S. Xiao, C. Hu, T. Zhang, X. Meng, H. Lin, Y. Yang, S. Yang, *Adv. Energy Mater.* **2017**, *7*, 1701038.
[52] P. Chen, Y. Bai, S. Wang, M. Lyu, J.-H. Yun, L. Wang, *Adv. Funct. Mater.* **2018**, *28*, 1706923.
[53] M. Tai, Y. Zhou, X. Yin, J. Han, Q. Zhang, Y. Zhou, H. Lin, *J. Mater. Chem. A* **2019**, *7*, 22675.
[54] C.-H. Yang, S.-B. Xiao, H. Xiao, L.-J. Xu, Z.-N. Chen, *ACS Nano* **2023**, *17*, 7830.